Analysis of Heat Pipes for CPC Solar Collectors to Provide Heat for Industrial Processes

Renzo Guido Cruz[1], Juan M. Rodriguez-Muñoz[2] and Pedro Galione Klot[1]

[1] School of Engineering, Universidad de la República, Montevideo (Uruguay)

[2] Department of Physics, CENUR Litoral Norte, Universidad de la República, Salto (Uruguay)

Abstract

As part of a project aimed at supporting medium-temperature industrial heat processes, this study analyzes the use of solar-concentrated Heat Pipes to reach steam-generation temperatures around 150 °C. The system employs a concentrator reflector with a concentration ratio of one and vacuum tubes to minimize thermal losses. A detailed thermal model was developed to compute the system's internal heat flows and temperatures. The model was validated using experimental data from a solar collector test bench following international standards. Different system configurations were compared, highlighting a 4% overall efficiency variation due to changes in Heat Pipe quality and a 13% improvement by changing the reflectors' properties.

Keywords: Solar Heat for Industrial Processes, Heat Pipes, Thermodynamics, Low-temperature steam.

1. Introduction

Solar Heat for Industrial Processes (SHIP) is becoming an increasingly relevant energy source for industries worldwide. Nevertheless, according to the SHC 2024 report (Weiss and Spörk-Dür, 2024), fossil fuels still account for 90% of the heat demand in industrial processes operating below 400 °C. This reveals a substantial opportunity for solar technologies to expand in this sector. Germany and Spain currently lead the global SHIP landscape, where many industries have already found it economically viable to replace fossil fuels with solar thermal technologies such as Fresnel and parabolic concentrators. Although Uruguay has a solar resource comparable to Spain, progress in SHIP adoption has been significantly slower, and solar heat has yet to penetrate the energy market.

This work is part of a larger project, whose objective is to take the first step toward replacing fuel oil with solar heat for low-temperature steam production (~150 °C) in Uruguay. Several tax incentives are currently in place to promote the use of renewable energy in industry, and this initiative is fully aligned with those policies. The project focuses on the design, construction, and testing of a prototype system capable of producing and storing heat at 100–150 °C, the first of its kind in the country. The prototype facility comprises the solar field, a concrete thermal energy storage unit, and a heat exchanger that simulates heat consumption at ~130 °C. The installation is currently under construction and is expected to become operational during the first half of 2026.

To transfer heat to the boiler, pressurized glycol-water will be used as the working fluid, circulating through a Compound Parabolic Collector (CPC) - Heat Pipes (HP) and Vacuum Tubes (VT) solar field. This type of solar collector was selected due to its relative simplicity (it does not require solar tracking), the local availability of heat pipes (commonly used in low-temperature solar water heaters), and its capability to deliver heat in the 100–150 °C range [Horta, 2016; McMillan et al., 2021; Kalogirou, 2013]. However, in order to achieve an adequate design and predict its performance, it is necessary to fully understand the collectors' thermal behavior and to quantify both the useful heat and thermal losses.

This study presents a thermal model of heat pipes for CPC solar collectors, providing a detailed analysis of the various thermal resistances involved in the heat transfer from the absorber surface to the working fluid, quantifying the relative contribution of each resistance. Also, a simple optical model was developed to address the optical efficiency problem. With experimental validation, this model serves as a valuable design tool, which was applied within the framework of the project to develop a specific design for SHIP applications. Additionally, a sensitivity analysis was conducted on this design, focusing on optimizing thermal performance.

This article is organized as follows. In Section 2, the thermodynamic and optical model developed for the CPC

collector with heat pipes is presented, along with the conditions under which it is considered valid. Section 3 presents the experimental validation using a prototype collector. Section 4 describes the final design developed within the project framework, as well as a sensitivity analysis of the design variables aimed at exploring enhanced thermal performance. Finally, Section 5 summarizes the main conclusions.

A general description of the overall project, along with detailed presentations of specific aspects such as the concrete thermal storage system, the optical design of the CPC collectors, and the experimental performance tests, are provided in other presentations within SWC 2025.

2. Thermodynamic model

Figure 1 shows a schematic of a section of the solar collector, illustrating its main components. Solar radiation passes through the vacuum tube and is absorbed by the collector either directly or after being reflected by the reflective plate. The absorbed energy is then conducted to the outer aluminum fins and subsequently transferred to the inner fins. From there, heat reaches the HP, where it causes the internal water to evaporate. The vapor travels to the condenser section, where it condenses on the inner walls of the condenser bulb. During condensation, latent heat is released and flows through the wall of the HP, the thermal paste, and into the copper socket, which is soldered to the manifold pipe. From the socket and the pipe, heat is transferred to the circulating water via forced convection.

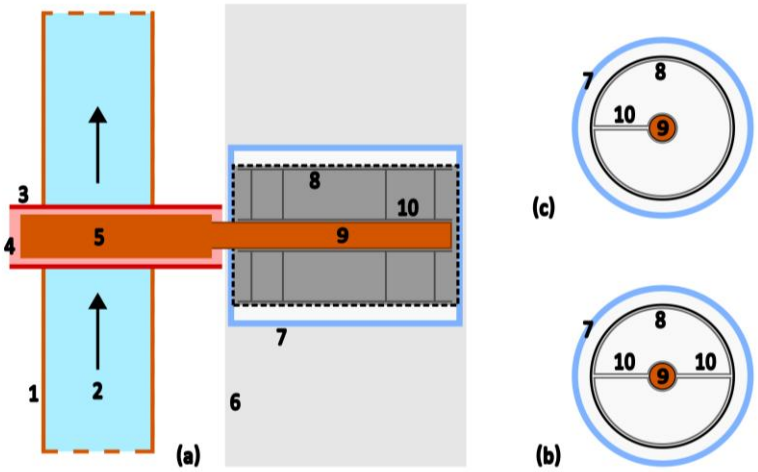

Figure 1: Scheme of a section of the manifold (without insulation) with one HP and a vacuum tube. a) Front view of the system. b) Cross-section view of type 2 VT. c) Cross-section view of type 1 VT. 1-Manifold. 2-Working fluid. 3-Socket. 4-Thermal paste. 5-HP condenser. 6-Reflective plate. 7-Vacuum tube. 8-Absorber. 9-HP evaporator. 10-Aluminum fins.

As the evaporator section is 1.715 m long while the condenser section is only 60 mm in height, the schematic may give a misleading impression of the system's proportions. The evaporator has a radius of 8 mm, the condenser 14 mm, the absorber 47 mm, and the vacuum tube features an outer radius of 58 mm. The design's concentration ratio (ratio between the aperture area, which is rectangular, and the absorber area, which is the sum of the areas of each individual cylindrical absorber surface) is one, so the reflective plate width is 147 mm, following the involute shape, as explained by O'Gallagher et al. (1980).

Since the collector consists of N identical sections, analyzing and optimizing a single unit, as illustrated in Figure 1, provides valuable insight into the system's overall behavior and performance.

Based on a detailed analysis of the manifold section, a thermal equivalent electrical circuit was developed to model heat transfer throughout the system, adapting the approaches proposed by Faghri (1995), Jack et al. (2011), and Shafieian et al. (2019). Figure 2 shows the resulting thermal resistance network, highlighting the main temperature nodes and the corresponding heat flow paths.

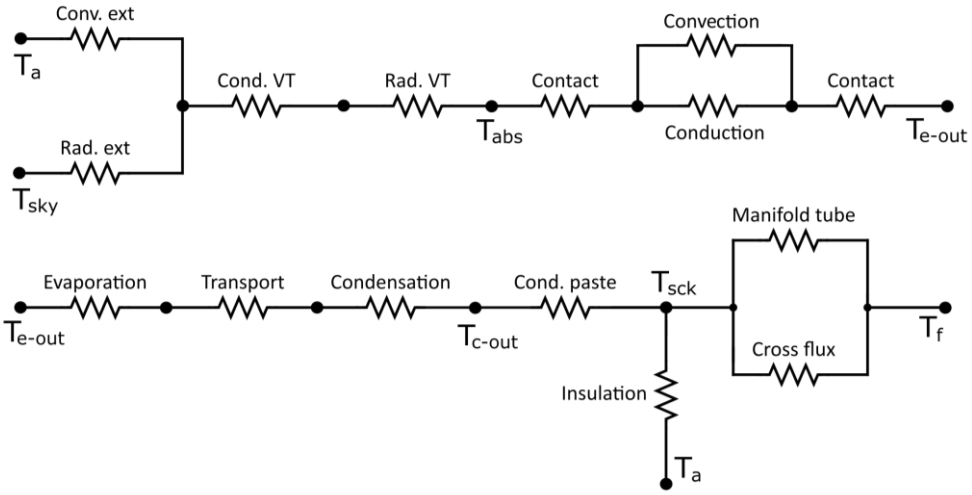

Figure 2: Electrical equivalent diagram of the temperatures and thermal resistances of the system.

For the thermal resistance of forced convection with the ambient air, Equation 1 WAS used. The correlation in equation 1 was taken from Jack et al. (2011) for the forced convection coefficient, h_{forz}^{amb}, linear to the wind speed. Heat transfer by radiation occurs in parallel, with the associated thermal resistance and the utilized sky temperature are described in Equations 2 and 3.

$$R_{conv}^{ext} = \left(h_{forz}^{amb}\, D_{VT}\, \pi\, L_{VT} \right)^{-1} \qquad \text{with } h_{forz}^{amb} = 5.7 + 3.8\, v_{wind} \qquad \text{(eq. 1)}$$

$$R_{rad}^{ext} = \left(\epsilon_g\, \sigma \left(T_{sky}^2 + T_{VT-ext}^2\right)\left(T_{sky} + T_{VT-ext}\right) \frac{1}{2} D_{VT}\, \pi\, L_{VT} \right)^{-1} \qquad \text{(eq. 2)}$$

$$T_{sky} = \epsilon_{sky}^{0.25}\, T_{amb} \qquad \text{where } \epsilon_{sky} = 0.75 \qquad \text{(eq. 3)}$$

Where the model for the sky temperature under clear sky conditions was obtained from Li et al. (2017), D_{VT} and L_{VT} are the diameter and the length of the HP, T_{VT-ext} is the temperature of the exterior face of the VT and ϵ_g is the emissivity of the glass that was set to 0.9.

The thermal resistance for conduction across the vacuum tube was modeled using the equation from Bergman et al. (2011) for concentric cylinders, shown in Equation 4. Furthermore, heat transfer by radiation within the vacuum tube was analyzed, with convection being neglected since the manufacturer guarantees the absence of enclosed air. For the outer tube, the emissivity of borosilicate glass was used, while for the inner tube (the absorber), the value provided by the manufacturer (7%) was applied. Equation 5 shows the resulting radiative heat transfer coefficient. From the sum of the aforementioned thermal resistances, the heat losses to the exterior can be obtained for a given absorber temperature.

$$R_{cond} = \ln\left(\frac{D_{TV-ext}}{D_{TV-int}}\right) \left(\kappa_g\, 2\pi\, L_{VT}\right)^{-1} \qquad \text{(eq. 4)}$$

$$h_{rad}^{abs} = \frac{\sigma \left(T_{VT-int}^2 + T_{abs}^2\right)\left(T_{VT-int} + T_{abs}\right) \frac{1}{2} D_{VT}\, \pi\, L_{VT}}{\frac{1}{\epsilon_{abs}} + \frac{A_{abs}}{A_{TV-int}} \left(\frac{1}{\epsilon_g} - 1\right)} \qquad \text{(eq. 5)}$$

Where κ_g is the glass thermal conductivity, T_{VT-int} is the tempeture of the inner face of the vacuum tube, T_{abs} is the temperature of the absorber, ϵ_{abs} its emissivity and A_{abs} and A_{TV-int} their areas. The absorber emissivity was uncertain and was therefore treated as a parameter during model validation. It was assumed that convection or conduction heat transfer between the absorber and the outer glass were negligible.

On the other hand, to determine the heat transfer from the absorber to the fluid, all the remaining resistances to the right and below in the schematic must be modeled. There were three resistances from the absorber to the outer wall of the evaporator, which geometry was presented in panels (b) and (c) in Figure 1. Two contact resistances were added: the first between the absorber wall and the aluminum fin, which is simply resting on the wall, and the second between the inner aluminum fin and the copper tube of the evaporator. This was calculated by Equation 6. The heat can be transferred from one fin to the other either through conduction in the aluminum or by convection through the air enclosed within the fins of the vacuum tube. For the conduction resistance, a simple plane wall model was used, while for the convection resistance, the correlation described in Bergman et al. (2011) for natural convection in

concentric cylinders was applied. The equations for the contact resistance and the heat transfer coefficient for concentric cylinders (h_{CC}) were given in Equations 6 and 7, respectively.

$$R_{fin} = \frac{1}{N_{fins}\, L_{ev}} \left(\kappa_{al}\, \delta\, m_{fin} \tanh\left(m_{fin}\, L_{fin}\right)\right)^{-1} \text{ where } m_{fin}^2 = \frac{U_{cont}}{\kappa_{al}\delta} \qquad \text{(eq. 6)}$$

$$h_{CC} = \frac{2\pi\,\kappa}{\ln\left(\frac{D_{abs}}{D_{ev}}\right)}\, 0.386 \left(\frac{\Pr\, Ra}{\Pr + 0.861}\right)^{0.25} \qquad \text{(eq. 7)}$$

Where κ, Pr and Ra are the thermal conductivity, Prandtl number, and Rayleigh number of air. L_{ev} and D_{ev} are the length and diameter of the evaporator, δ is the thickness of the aluminum fin, and U_{cont} is the heat transfer coefficient of contact.

Once heat reaches the outer wall of the evaporator, the heat pipe (HP) was designed to transfer it to the condenser with minimal losses. In this model, the HP was simulated following the proposals from Abi Mathew and Thangavel (2021) and Shafieian et al. (2019), where the phase-change heat transfer coefficients (h_{FC}) were calculated using Equation 8, sourced from Bergman et al. (2011).

$$h_{FC} = 0.728 \left(\frac{g \sin(\theta)\, \rho_l\, (\rho_l - \rho_v)\, \kappa^3\, h_{fg}}{D\, \mu_l\, \Delta T}\right)^{0.25} \qquad \text{(eq. 8)}$$

Where g is the gravitation acceleration, θ is the inclination angle of the HP, ρ_l and ρ_v are the liquid and vapor densities, κ and μ_l are the thermal conductivity and dynamic viscosity of the liquid phase, h_{fg} is the evaporation enthalpy, and ΔT is the temperature difference between the fluid and the wall. The values for these coefficients in both the evaporator and condenser regions were above 10^4 W m^{-2}K^{-1}.

Finally, the thermal resistance between the condenser wall and the working fluid must be modeled. The first thermal resistance is conduction through the thermal paste, represented by Equation 9. It is important to note that this equation is only valid when the thermal paste is uniformly applied across the entire gap between the sleeve and the condenser. A uniform gap and the absence of manufacturing defects were also assumed. If air were present instead of thermal paste, the thermal resistance would increase significantly, governing the overall heat transfer to the fluid.

$$R_{cond} = \ln\left(\frac{D_{sck-int}}{D_{CB}}\right)\left(\kappa_p\, 2\pi\, L_{CB}\right)^{-1} \qquad \text{(eq. 9)}$$

Where $D_{sck-int}$ and D_{CB} are the inner diameter of the socket and the outer diameter of the condensation bulb, respectively, the difference between them being twice the gap width, which is filled with the thermal paste of conductivity κ_p. L_{CB} is the length of the condensation bulb.

To model the heat transfer from the socket, losses through the insulation were considered on one side, and the useful heat transferred to the working fluid on the other. This useful heat reaches the working fluid through two paths. The first is a direct transfer from the socket via forced convection to the fluid, modeled as cross-flow according to Equation 10, extracted from Bergman et al. (2011).

$$h_{cf} = 0.21\, \kappa\, Pr^{0.38}\, Re^{0.62}\, D_{sck}^{-1} \qquad \text{(eq. 10)}$$

The second path is through the manifold, which acts as a fin. Assuming a constant convection coefficient along the tube, this fin can be solved analytically under the assumption that the tube wall is sufficiently thin to neglect the difference between its outer and inner diameters. The analytical solution for the temperature profile, applied to a cylinder at constant temperature with a uniform coefficient h, was also taken from Bergman et al. (2011). Equation 11 presents the profile for a unit temperature difference between the socket and the fluid. This profile depends on the tube thickness, its conductivity, and the coefficient h. The method of images was used to adapt this analytical solution to the tubes heated by the heat pipes.

$$T(r) = K_v(0, mr)\, \left(K_v(0, m\, R_{sck})\right)^{-1} \text{ with } m^2 = \frac{h}{\kappa_{cu}\, t} \qquad \text{(eq. 11)}$$

Where $K_v(0)$ is the second type Bessel function of order zero, h is the turbulent flow heat transfer coefficient for pipes taken from Duffie et al. (2020), t is the thickness of the manifold, and κ_{cu} is the thermal conductivity of copper.

By imposing a known heat input to the absorber, all these thermal resistances can be solved to determine both the heat loss from the absorber to the environment and the useful heat that reaches the working fluid. This yields the thermal efficiency for a single Reflector + Heat Pipe. The model was then generalized for the entire collector, composed of N consecutive heat pipes.

Furthermore, a straightforward optical efficiency model was developed to couple with the thermodynamic model. This model is discussed in detail in another presentation within SWC 2025. For normal incidence, the optical efficiency can be approximated by Equation 12. This equation assumes the absorptivity and transmissivity of the glass and the selective surface are uniform in all directions. It also depends on the reflectivity parameter of the mirrored stainless steel, whose value was measured in the laboratory but was treated as an adjustable parameter to account for potential imperfections in the reflector's construction.

$$\eta_{opt} = \frac{1}{w}(\tau\alpha D_{abs} + R_{ss}\tau^3\alpha(D_{VT} - D_{abs}) + R_{ss}\tau\alpha(w - D_{VT})) \qquad \text{(eq. 12)}$$

Where w is the width of the reflector, τ is the transmissivity of the VT, α is the absorptivity of the absorber, and R_{ss} is the effective reflectivity of the stainless steel. This model can be easily understood by looking at Figure 3, where the first term between the brackets corresponds to the amount of energy that goes directly to the absorber, the second terms goes twice through the VT and then bounces back and reaches the absorber, and the third term in the brackets corresponds to the energy that goes from the sun to the reflector and then to the absorber. This equation holds true while the concentration ratio is small enough, so the solar rays just bounce once in the reflector, and that was the case for the validation test.

3. Experimental validation

A prototype collector, very similar to the proposed design but with a lower concentration ratio, was tested at the Solar Energy Laboratory (LES, http://les.edu.uy/) of the Universidad de la República (UdelaR), to validate the model and adjust the unknown parameters. The facility is located near the city of Salto, Uruguay (latitude: 31.28° S, longitude: 57.92° W), and the test installation complies with all the requirements of ISO 9806 (2017). The performance test was conducted in accordance with the steady-state test method proposed in this standard, ensuring steady-state conditions, clear sky, and normal incidence. The experimental parameters η_0, a_1, and a_2 were calculated. These parameters were defined by Equation 13. The model was validated by comparing the experimental efficiency curve with the modeled curve, using the reflectivity of the stainless steel, the contact coefficient U_{cont} between the aluminum and copper, and the absorber emissivity as fitting parameters.

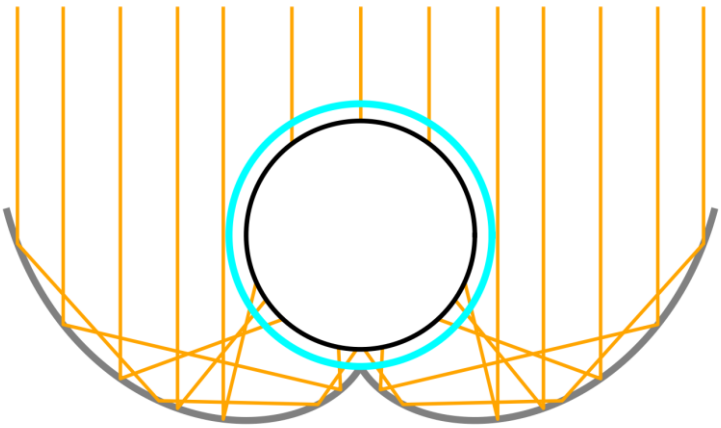

Figure 3: Scheme of the path taken by solar rays in normal incidence to the absorber. This represents the future absorber.

$$\dot{Q}_{use} = \eta_0\, G\, A_{ap} - a_1 A_{ap}\left(T_f - T_{amb}\right) - a_2 A_{ap}\left(T_f - T_{amb}\right)^2 \qquad \text{(eq. 13)}$$

Given the smaller reflector, it was assumed that all solar rays incident on the reflector undergo only a single reflection before reaching the absorber. This minimizes optical misalignment and allows for the determination of the reflectivity coefficient of the mirrored stainless steel under typical Uruguayan solar conditions. The parameter R was allowed to vary between 0.5 and 0.6, consistent with measurements obtained in the optics laboratory. The coefficient U was permitted to vary between 300 and 2500 W $m^{-2}K^{-1}$, aligning with the ranges suggested by Bergman et al. (2011). The absorber emissivity was allowed to vary between 5% and 10%.

The minimum RMSD was achieved with the values $\epsilon_{abs} = 0.075$, $R_{ss} = 0.56$, and $U_{cont} = 700\ Wm^{-2}K^{-1}$, none of which were at the boundary of the parameter space. A comparison between the simulated and experimentally obtained efficiency curves is shown in Figure 4. The RMSD was 0.35%.

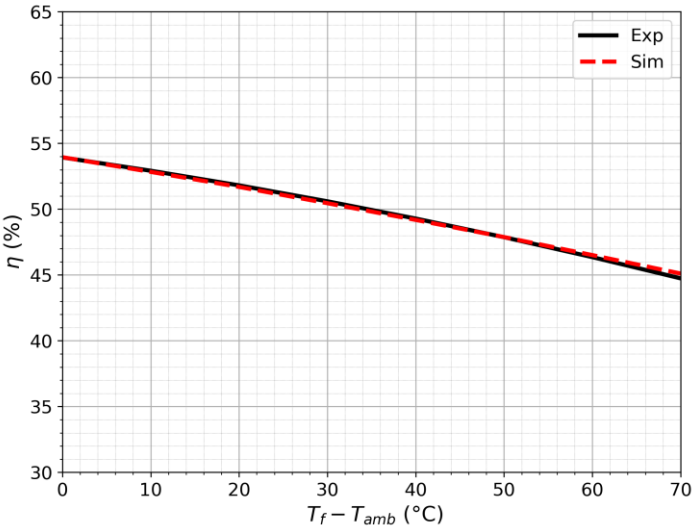

Figure 4: Comparison between experimental and simulated efficiency curves when G=1000 Wm^{-2}.

4. Results and analysis

The validated model presented and experimentally verified in the previous section constitutes a valuable design tool within the framework of the aforementioned project. In this regard, the model for the higher concentration ratio was developed using validated input parameters ($\epsilon_{abs} = 0.075, U_{cont} = 700\ Wm^{-2}K^{-1}, \eta_0$). The optical efficiency for the new reflector was calculated using Tonatiuh, a well-known open-source program for solar systems, which enabled the consideration of double reflections within the reflector.

To achieve a better understanding of the collector's behavior and optimize its design, the thermal resistance circuit was solved for various working fluid temperatures under standard climate conditions defined by an ambient temperature of 20°C and typical clear-sky irradiance conditions (G = 1000 W/m², f_o = 0.15). This analysis determined the temperature at each node as a function of the working fluid temperature, along with the useful heat output, thermal losses, and overall system efficiency. To maximize efficiency, the absorber temperature must be minimized for a given heat flux, which was achieved by minimizing the thermal resistances along the heat transfer path. A sensitivity analysis was performed on key system parameters, including flow rate, manifold thickness, thermal paste properties, the quality of the HPs and VTs, and reflectivity.

Figure 5 presents two case studies comparing the performance of HPs and VTs of different quality levels. The Type 1 configuration (left) features four thicker fins, while Type 2 (right) has two thinner fins, with all other system components remaining identical. The absorber temperature in the lower-quality configuration (Type 1) is higher for a given fluid temperature. The temperature gradients between the absorber (black), evaporator outer wall (red), condenser outer wall (orange), and working fluid (blue) correspond to the thermal resistance in each section. Within the HPs, the temperature difference between the evaporator and condenser is minimal, consistent with findings from Jack et al. (2011) under standard operation, as evidenced by the proximity of the red and orange curves.

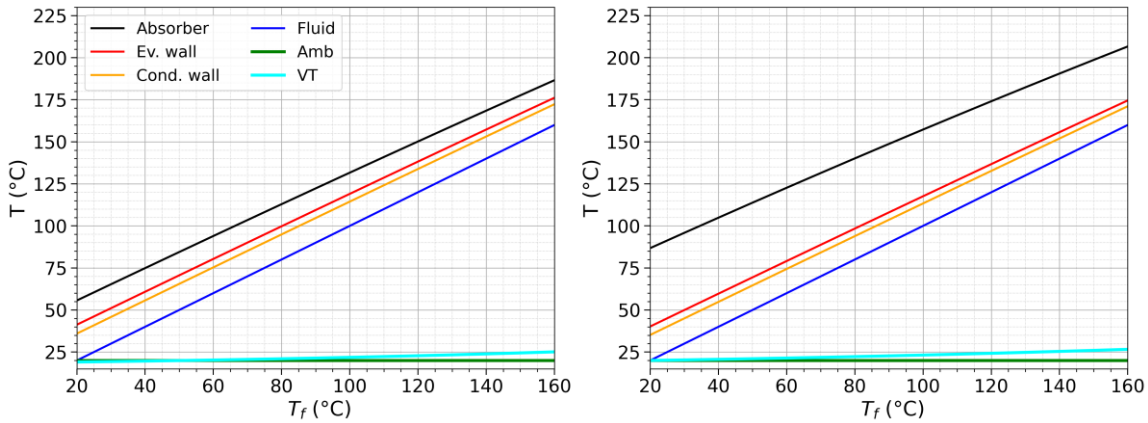

Figure 5: Temperatures of different nodes as a function of the working fluid temperature. Left: Type 1 HP; Right: Type 2 HP.

In the left panel, the black and blue lines maintain similar distances from the other curves, indicating that reducing

thermal resistances either from the absorber to the evaporator or from the condenser to the working fluid would similarly enhance system performance. In the right panel, the greater separation of the black curve suggests a significant thermal bottleneck between the absorber and the HP. The Type 2 arrangement requires a larger temperature differential due to its inferior fin thermal conductance.

Since heat losses from the absorber depend on its operating temperature, a higher absorber temperature directly reduces system efficiency for a given energy input to the vacuum tube. Figure 6 shows efficiency as a function of fluid temperature, where dashed lines represent the Type 2 HP configuration and solid lines represent Type 1. Both thermal and overall efficiencies are presented, showing visibly lower thermal performance for Type 2, which consequently degrades the overall system efficiency. The net result indicates that using higher quality heat pipes (Type 1) can achieve overall efficiencies 4% greater in the operational temperature range (120 to 160°C), resulting in approximately 10% higher useful energy yield. This improvement stems from a 7% difference in thermal efficiency within the same range. The figure also shows the optical efficiency (green) of 51% and additional losses in the manifold.

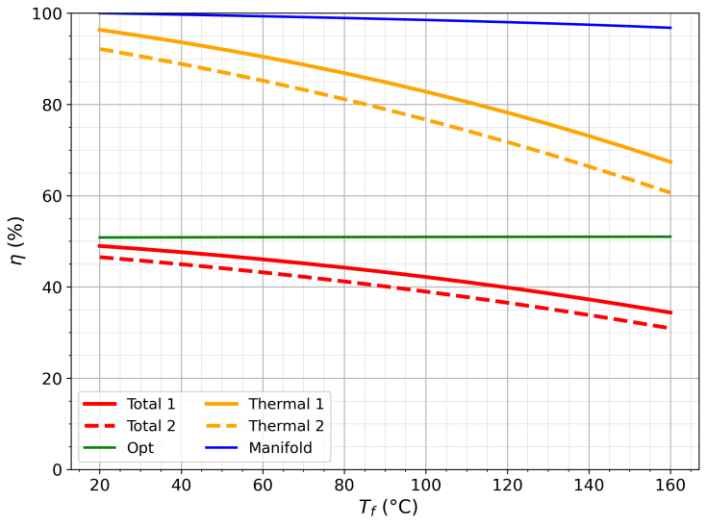

Figure 6: Differences in overall efficiencies for different Heat Pipes.

Another area identified as critical in the thermal system was the proper application of the thermal paste between the condenser bulb and the socket. This gap is small but can introduce significant thermal resistance if the paste is incorrectly applied or degrades over time. According to manufacturer specifications, the thermal paste should have a conductivity of approximately 1 $W \cdot m^{-1} \cdot K^{-1}$. The system's behavior was analyzed for four degradation scenarios: the design case (black) with 1 $W \cdot m^{-1} \cdot K^{-1}$, a lower conductivity case (red) with 0.25 $W \cdot m^{-1} \cdot K^{-1}$, a lowest conductivity case (orange) with 0.075 $W \cdot m^{-1} \cdot K^{-1}$, and a no-paste scenario (blue) with air conductivity (0.025 $W \cdot m^{-1} \cdot K^{-1}$).

The reduction in thermal conductivity may result from air pockets within the paste or material deterioration, as indicated in studies by Jack et al. (2011). Figure 7 shows the absorber temperature under these conditions (left panel) and the corresponding impact on system efficiencies (right panel). The difference between the design case and the lower degradation case is minimal, approximately 1% in thermal efficiency. However, significant degradation (orange) has a much more pronounced effect on system performance. In the complete absence of thermal paste, system operation becomes severely compromised.

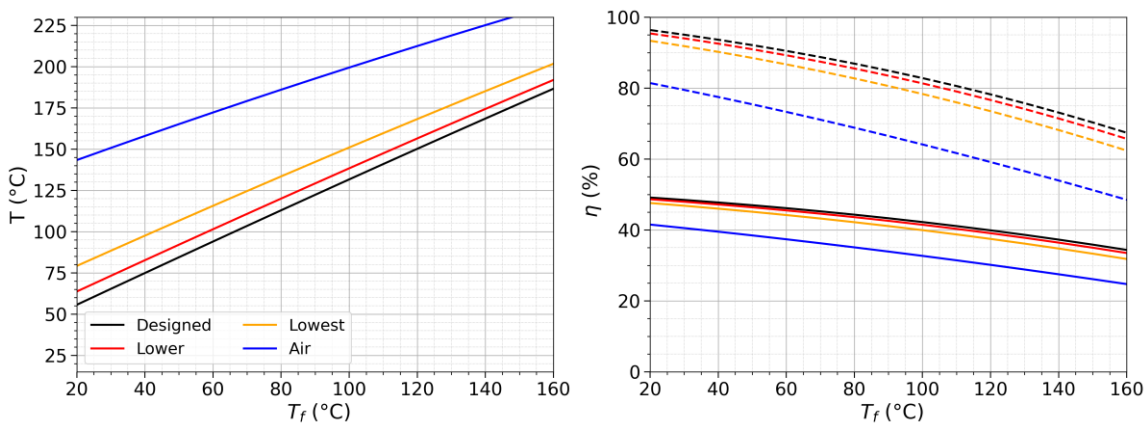

Figure 7: Differences in overall efficiencies as thermal paste deteriorates.

Another operational parameter that could be critical during operation is the flow rate through the manifold. The nominal flow rate is 6.4 L/min, circulating through a circular manifold with an inner diameter of 26.8 mm. The resulting mean flow velocity is 0.2 m/s, which strongly influences the convection coefficient between the fluid and both the tube and the socket, thereby reducing the thermal resistance from the condenser to the fluid. Simulations were performed for the same manifold dimensions with a 50% increase (orange) and a 50% decrease (red) from the original flow rate. The results are shown in Figure 8, where the left panel displays the absorber temperatures and the right panel shows the corresponding efficiencies.

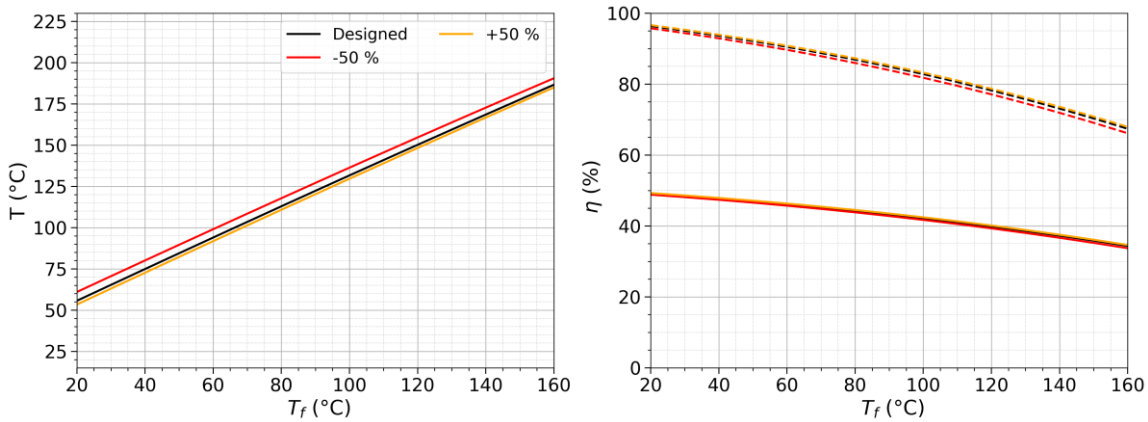

Figure 8: Differences in absorber's temperature and efficiencies as the flow rate varies.

The observed temperature variations were minimal, in the order of a few degrees in the absorber, and consequently, the changes in efficiency were also very small. The flow rate would need to be multiplied several times to have an appreciable effect on the overall system performance.

Finally, using Tonatiuh, the system's behavior was analyzed for changes in the reflector's reflectivity, which would logically entail using a different base material. A switch to mirrored aluminum for solar applications, with a laboratory-measured reflectivity of ~85%, was considered. To account for construction imperfections and practical details, an effective reflectivity of 80% was simulated. An intermediate case between the stainless steel (56%) and the aluminum was also simulated, with a reflectivity fixed at 68%.

The Tonatiuh simulations yielded optical efficiencies of 51.0%, 57.6%, and 65.1% for these cases, respectively. These efficiencies directly alter the amount of energy reaching the absorber. While the increased energy input raises the absorber temperature and thus the thermal losses, the reduction in optical losses was even more significant. Figure 10 shows the resulting absorber temperature differences, which were only a few degrees, compared to the substantial differences in total system efficiency—over 10% between the 80% reflectivity case (blue curve) and the original case (black curve).

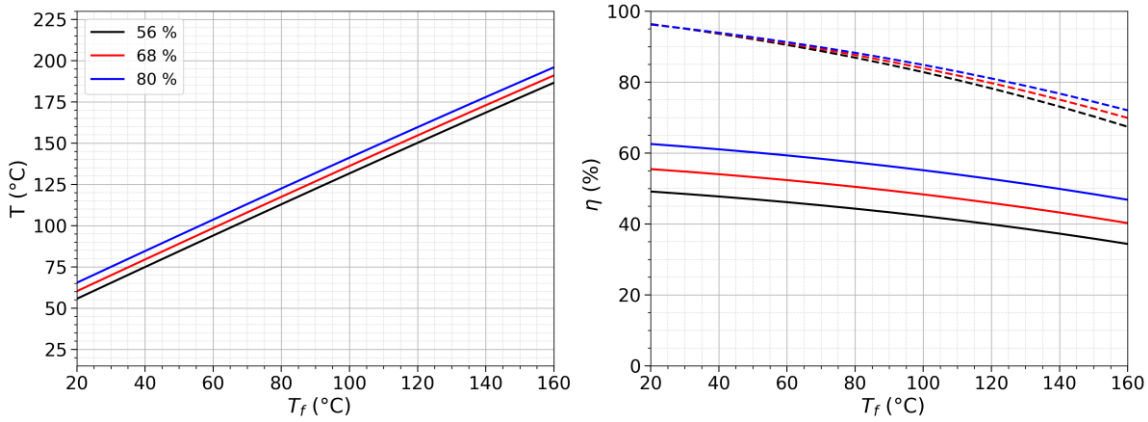

Figure 9: Differences in absorber temperatures and efficiencies for several reflectivities.

It is also noteworthy that, despite the higher absorber temperature in the high-reflectivity case, the thermal efficiency is superior. This occurs because the net increase in thermal losses is outweighed by the greater amount of heat effectively transferred to the working fluid.

5. Conclusions & Perspectives

A thermal model was developed for the CPC-HP-VT solar system. The model was calibrated using a reflector with a concentration ratio of 0.73 and was subsequently extended to a solar system with a unit concentration ratio. The calibrated parameters were found to fall within the expected ranges reported in the literature.

The project is currently in the prototype construction phase. The forthcoming results will be valuable for further model validation and final adjustments before the production of the final modules. To summarize the study's findings, Table 1 presents the impact of each modification — from best to worst — on the thermal, optical, and overall efficiencies, evaluated at a fluid temperature of 140 °C. In all cases, the modified system was compared with the baseline design, which incorporates the Type 1 heat pipe (higher quality), standard non-degraded thermal paste, a flow rate of 6.4 L/min, and a stainless-steel reflector.

Table 1: Impact on the efficiencies of the system of the changes studied.

Proposed change	Optical efficiency	Thermal efficiency	Overall efficiency
Improved reflectivity to 80%	Improve 13%	Improve – 3.7%	Improve – 12.6%
Improve reflectivity to 68%	Improve 6.7%	Improve – 2.0%	Improve – 6.0%
Increased 50% the flow rate	Unchanged	Improve – 0.3%	Improve – 0.5%
Decreased 50% the flow rate	Unchanged	Worsen – 1.2%	Worsen – 0.6%
Thermal paste degradation – Lower	Unchanged	Worsen – 1.7%	Worsen – 0.8%
Thermal paste degradation – Lowest	Unchanged	Worsen – 4.9%	Worsen – 2.5%
Low-quality VT and HP	Unchanged	Worsen – 6.5%	Worsen – 3.3%
Thermal paste degradation - Air	Unchanged	Worsen – 19.2%	Worsen – 9.8%

As shown in the table, variations in flow rate are not expected to significantly affect system performance. Although severe degradation of the thermal paste could adversely impact operation, this is unlikely to occur with proper maintenance. One of the most influential factors is the amount and thickness of the aluminum fins connecting the glass to the evaporator within the heat pipe tubes. Fewer and thinner fins increase the thermal resistance between the absorber and the heat pipe evaporator, which is expected to reduce overall performance by 3–4%. The greatest opportunity for improvement lies in replacing the reflector material with a more reflective alternative, although this decision ultimately depends on the cost of reflective aluminum.

6. Acknowledgments

The authors extend their gratitude to VOLFER Metal-Mechanic Industry for their collaboration in developing this product for the Uruguayan market. We also acknowledge the financial support provided by the National Agency for Research and Innovation (ANII).

7. References

Abi Mathew, A., & Thangavel, V. (2021). A novel thermal storage integrated evacuated tube heat pipe solar air heater: energy, exergy, economic and environmental impact analysis. Solar Energy, 220, 828-842.

Bergman, T. L., Lavine, A. S., Incropera, F. P., & DeWitt, D. P., 2011. Introduction to heat transfer. John Wiley & Sons.

Duffie, J. A., Beckman, W. A., & Blair, N., 2020. Solar engineering of thermal processes, photovoltaics, and wind. John Wiley & Sons.

Faghri, A., 1995. Heat pipe science and technology. Global Digital Press.

Horta, P., Brunner, Ch., Kramer, K., Frank, E. (2016). IEA/SHC T49 Activities on Process Heat Collectors: Available

Technologies, Technical-Economic Comparison Tools, Operation and Standardization Recommendations. Energy Procedia 91, 630-637.

ISO 9806. (2017). Solar energy – Solar thermal collectors – Test methods. International Organization for Standardization.

Jack, S., Katenbrink, N., & Schubert, F., 2011. Evaluation Methods for Heat Pipes in Solar Thermal Collectors - Test Equipment and First Results. In the ISES solar world congress (Vol. 28).

Kalogirou, S. A., 2013. Solar Energy Engineering. Chapter 3 Solar Energy Collectors. Elsevier, 2013.

McMillan, C., Schoeneberger, C., Zhang, J., Kurup, P., Masanet, E., Margolis, R. Meyers, S., Bannister, M., Rosenlieb, E., and Xi, W.. 2021. Opportunities for Solar Industrial Process Heat in the United States. Golden, CO: National Renewable Energy Laboratory. NREL/TP-6A20-77760.

O'Gallagher, J. J., Winston, R., Rabl, A., & McIntire, W., 1980. Absorption enhancement in solar collectors by multiple reflections. Solar Energy, 24(3), 323-326.

Shafieian, A., Khiadani, M., & Nosrati, A. (2019). Theoretical modelling approaches of heat pipe solar collectors in solar systems: A comprehensive review. Solar Energy, 193, 227-243.

Weiss, W., & Spörk-Dür, M., 2024. Solar Heat Worldwide: Edition 2024. IEA Solar Heating & Cooling Program. DOI: 10.18777/ieashc-shww-2024-0001.